A CONSTITUTIVE MODEL OF SANDSTONE CONSIDERING THE POST PEAK BEHAVIOR

F. S. Jeng

Department of Civil Engineering
National Taiwan University
Taipei, Taiwan

M. C. Weng*

Department of Civil and Environmental Engineering
National University of Kaohsiung
Kaohsiung, Taiwan

Department of Civil Engineering
National Chiao Tung University
Hsinchu, Taiwan

F. H. Yeh **Y. H. Yang** **T. H. Huang**

Department of Civil Engineering
National Taiwan University
Taipei, Taiwan

ABSTRACT

In rock engineering, evaluating the post-peak strength and deformation of rock is necessary. To explore the elasto-plastic behavior of sandstone in the post-peak stage, a series of strain-controlled triaxial tests were conducted under different confining pressures. According to the post-peak characteristics, a constitutive model based on nonlinear elasticity and generalized plasticity is proposed. This proposed model is characterized by the following features: (1) Nonlinear elasticity is observed under hydrostatic and shear loading; (2) the associated flow rule is followed; (3) substantial plastic deformation occurs during shear loading; and (4) post-peak softening behavior is accurately predicted. This model requires twelve material parameters, three for elasticity and nine for plasticity. The proposed model was validated by comparing the triaxial test results of Mushan sandstone at different hydrostatic pressures under dry and saturated conditions. In addition, the model is versatile; it can simulate the deformational behavior of two other sandstones. In summary, the proposed model can reasonably predict the complete stress–strain curve of sandstone.

Keywords: Constitutive model, Generalized plasticity, Post-peak behavior, Sandstone.

1. INTRODUCTION

The complete stress–strain curve of a rock represents that the displacement variations of rock undergo compressive loading from the pre-peak elastic phase to the ultimate compressive strength, and softening to the post-peak phase and, finally, approaching the residual strength. As the rock achieves the peak strength, the strength quickly decreases, and deformation significantly increases. In rock engineering, evaluating the post-peak bearing capacity and deformation is crucial. For example, in western Taiwan, weak sandstone undergone through juvenile rock forming process was often encountered during tunnel constructions. These materials exhibited relatively low shear strength and stiffness. In several unsuccessful tunneling projects constructed in weak rock strata, ground squeezing and tunnel face instability have been reported [1]. The inward squeezing easily occurred at the lower part of sidewall due to the post-peak softening after the excavation. Therefore, investigating the post-peak behavior to analyze the stability of excavation in a rock mass is essential. In addition, the long-term stability of underground excavation is related to the post-peak characteristics of surrounding

* Corresponding author (mcweng@nuk.edu.tw; mcweng@nctu.edu.tw)

DOI : 10.1017/jmech.2017.71
Copyright © 2017 The Society of Theoretical and Applied Mechanics
https://doi.org/10.1017/jmech.2017.71 Published online by Cambridge University Press

rock, such as creep deformation, fatigue damage, and damage of the support column after excavation [2]. To understand the mechanism of these stability problems, acquiring the complete stress–strain curves of a rock under different confining pressures is necessary.

To obtain the deformational behavior of sandstone under different confining pressures, the triaxial compressive test is commonly used [3-8]. However, reports providing satisfactory results regarding post-peak behavior, including axial and radial strains, are rare. [9] used Red Wildmoor sandstone as a specimen and performed conventional triaxial tests in the confining pressure range 1.4-10.3 MPa. Their study provided a series of complete stress–strain curves with high quality. The results indicated that the radial strain is low in the pre-peak stage; however, it develops significantly in the post-peak stage. Similar results were reported by [10], who conducted triaxial compression tests of Huabei greywacke to acquire complete stress–strain curves. The results showed that during low stress, axial and radial strain curves are fairly linear, and the axial strain is much greater than the radial strain. When the stress approaches the peak strength, the two strains, particularly the radial strain, increase rapidly. In the post-peak stage, the axial stress apparently decreases and the strain continues increasing until the stress achieves the residual strength. Moreover, they found that the variation in the axial strain is significantly affected by confining pressure, whereas the effect of confining pressure on the radial strain is insignificant. According to these results, this study established a constitutive model for predicting the complete stress–strain relationship of sandstone.

The theory of generalized plasticity was introduced by [11] to simulate soil behavior and later elaborated by [12] and [13]. Many studies have further developed a series of constitutive relations based on this framework to describe more sophisticated features of soil behavior [14-18]. Other than soils, [19] and [20] adopted the generalized plasticity concept with nonlinear elasticity in exploring rock behavior. Their models produce reasonable predictions of the elasto-viscoplastic deformation of sandstone under various confining pressures and stress paths and cyclic loadings. However, the previous models emphasize the prediction of the pre-peak behavior, and modeling the post-peak behavior is still incomplete. To further extend the capacity of this model to post-peak behavior, this study conducted a series of strain-controlled triaxial tests under different confining pressures, and the elasto-plastic characteristics of sandstone in the post-peak stage were explored. Based on the analysis results of post-peak behavior, the proposed constitutive model was established and is characterized by the following features: (1) Nonlinear elasticity is observed under hydrostatic and shear loading; (2) the associated flow rule is obeyed; (3) substantial plastic deformation occurs during shear loading; and (4) post-peak softening behavior is accurately predicted. After the model was formulated, the proposed constitutive model was validated by comparing the simulated and actual deformation of different sandstones under various stress conditions.

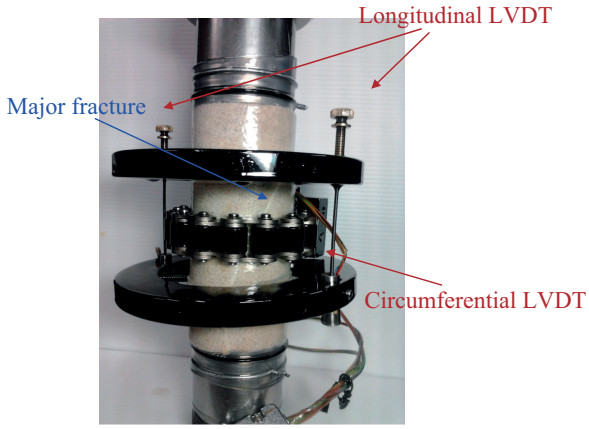


Fig. 1 Measurement of the axial and radial strains of a rock specimen. Two longitudinal LVDTs and one circumferential LVDT were set up to obtain the axial and radial deformation in a triaxial test.

2. EXPERIMENTAL SETUP

2.1 Specimen Preparation

This study examined Mushan sandstone (MS), a typical weak rock commonly found in the mountainous areas of northern Taiwan. The porosity of the sampled specimen is approximately 14.7%, and the dry density is approximately 2.28 g/cm^3. The average uniaxial compressive strength is 37.1 MPa under dry conditions and 28.9 MPa under saturated conditions. Petrographic analysis has shown that MS sandstone consists of 90.7% quartz and 9.0% rock fragments and is classified as lithic greywacke [21, 22].

Cylindrical specimens used for triaxial experiments were cored from a rock block in the same orientation with a diameter of 55 mm and a height of 129 mm. The experiments were conducted using dry and saturated specimens at room temperature. To establish the dry condition, the specimens were oven-dried for 24 hours at 110°C. To establish the saturated condition, the specimens were saturated with distilled water for 14 days in a vacuum chamber. The water content was measured every day. As the water content did not increase, the specimen was regarded as saturated.

2.2 Apparatus and Experimental Setup

To investigate the deformation characteristics of the weak sandstone, the experiments were performed using rock servo-controlled triaxial equipment [23]. The experimental setup is described as follows. The axial load was provided by a loading frame with a maximum capacity of 4500 kN; the loading rates were 0.001–30 mm/min. A triaxial cell can sustain a hydrostatic pressure of up to 140 MPa. Both axial and hydrostatic stresses were servo-controlled to enable conducting tests with various stress paths. To measure the deformation of the specimen, two longitudinal linear variable differential transformers (LVDTs) were set up to obtain the axial deformation, and one circumferential LVDT was configured to obtain the radial deformation (Fig. 1).

https://doi.org/10.1017/jmech.2017.71 Published online by Cambridge University Press

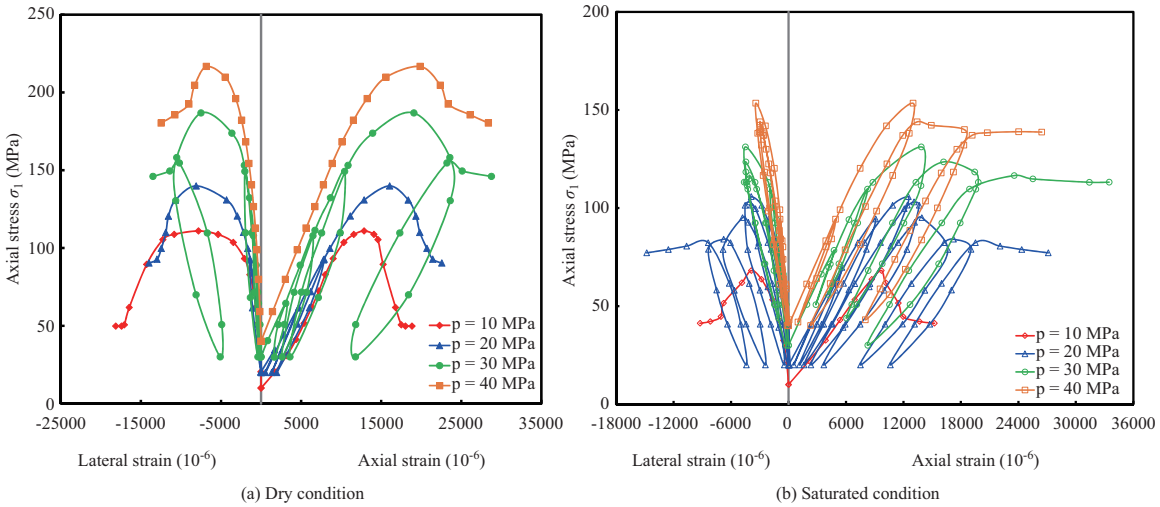


Fig. 2 Measured stress–strain curves of the CTC tests under various confining pressures. The term "p" represents the confining pressure.

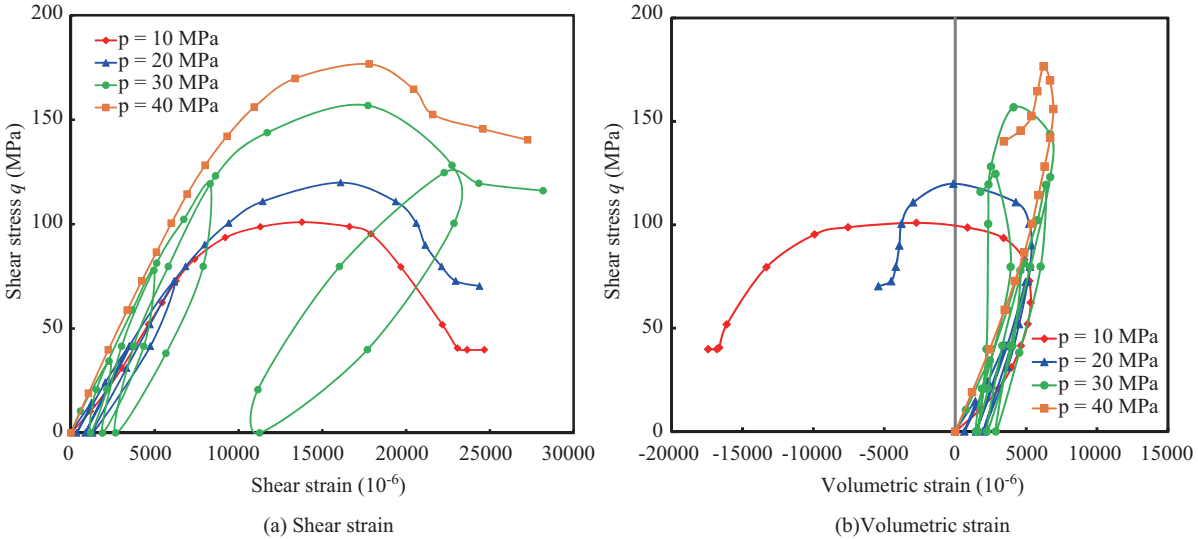


Fig. 3 Shear and volumetric strain curves under shear stress.

The accuracy of LVDTs is 0.002 mm.

The triaxial tests were designed by considering engineering applicability; therefore, the confining pressure ranged from 10 to 40 MPa. Therefore, the experimental data should be applicable to a wide range of engineering projects. The conventional triaxial compressive (CTC) path was followed in all tests, and the axial load was subsequently applied at a displacement rate of 0.02 mm/min. Furthermore, a test with the medium confining pressure was conducted using multiple unloading–reloading procedures to distinguish and separate elastic from inelastic deformation. This procedure included at least three cycles of unloading and reloading, and the three unloading cycles were initiated at 30%, 55%, and 80% of the ultimate strength.

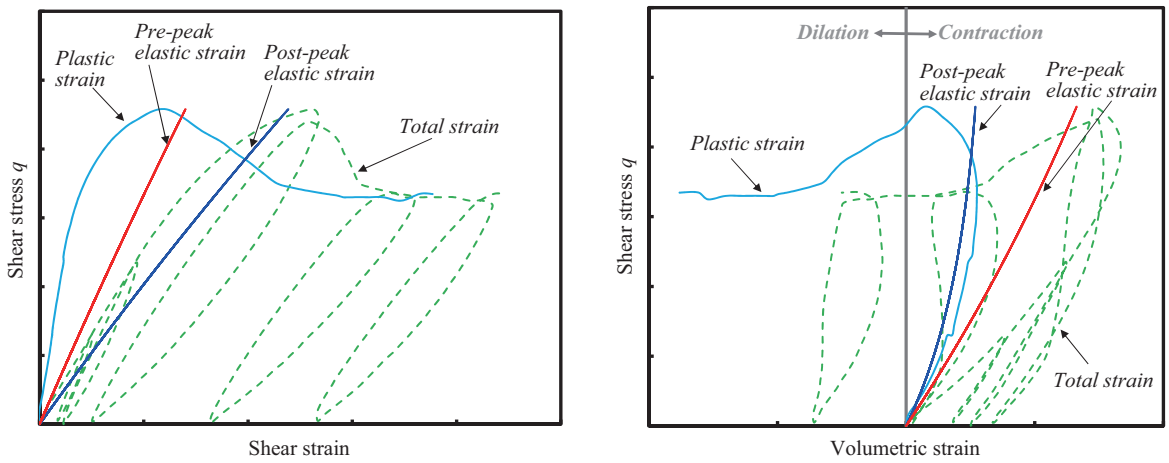
3. EXPERIMENTAL RESULTS

3.1 Elasto-Plastic Deformation of Sandstone

Figure 2 illustrates the stress–strain curves of the CTC tests under different confining pressures. For the dry specimens (Fig. 2(a)), the axial strain curves are generally linear at an earlier stage, and the initial stiffness increases in conjunction with the applied confining pressure. When the stress approaches the failure state, the strain exhibits significant brittle behavior. As the confining pressure increases from 10 to 40 MPa, the post-peak softening behavior becomes less significant. The stress drop decreases from 55.1 to 16.8%, which indicates the post-peak behavior converts from brittle to ductile state. Compared with the axial strain, the radial strain is much lower in the pre-peak stage; however, the radial strain develops significantly after the peak strength is achieved. Similar behavior is evident for the saturated specimens (Fig. 2(b)), except that the deformation of the saturated specimens is larger.

The axial and radial strain curves were converted into shear and volumetric strain curves under the applied shear stress (Fig. 3). The shear stress is defined as

https://doi.org/10.1017/jmech.2017.71 Published online by Cambridge University Press



(a) Shear strain (b) Volumetric strain

Fig. 4 Illustration of elastic and plastic strains during a CTC test.

$$q = \sqrt{3J_2}\,, \tag{1}$$

where J_2 is the second deviatoric stress invariant ($J_2 = \frac{1}{2}s_{ij}s_{ji}$, where s_{ij} is the deviatoric stress tensor). The shear strain and volumetric strain are presented in Eqs. (2) and (3), respectively.

$$\gamma = 2\sqrt{J_2'}\,/\sqrt{3}\,, \tag{2}$$

$$\varepsilon_v = \varepsilon_{kk}\,. \tag{3}$$

The post-peak shear strain is mainly affected by axial deformation and increases with an increase in the confining pressure, whereas the post-peak volumetric strain is mainly dominated by radial deformation and decreases with an increase in the confining pressure.

To investigate the elasto-plastic characteristics, the total strain tensor can be decomposed into the two components:

$$\varepsilon_{ij} = \varepsilon_{ij}^e + \varepsilon_{ij}^p\,, \tag{4}$$

where ε_{ij}, ε_{ij}^e, and ε_{ij}^p are the total strain tensor, elastic strain tensor, and plastic strain tensor, respectively.

According to the unloading–reloading curves at different stress stages, the relationship between shear stress and elastic strain can be obtained. The plastic strain can then be computed by subtracting the elastic strain from the total strain. Figure 4 illustrates the variation in elastic and plastic strains during a CTC test. For the shear strain (Fig. 4(a)), the variation in the elastic component is relatively linear, and it dominates the total deformation prior to the peak strength. The elastic shear stiffness increases with increasing hydrostatic pressure applied. When the stress approaches the peak strength, the plastic shear strain significantly increase; the plastic strain further grows in the post-peak stage. In addition, the post-peak elastic stiffness degrades compared with the pre-peak elastic stiffness. Figure 4(b) shows the variations in volumetric strain. The total strain causes contraction followed by significant dilation as the stress approaches the peak strength, and it continues to dilate in the post-peak stage. The plastic strain exhibits a similar tendency. However, the elastic deformation shows compression during the whole shearing process.Variations in the plastic strain increments can be further obtained using plastic strain curves. The dilatancy is defined on the basis of both the volumetric and shear strain increments and is shown as

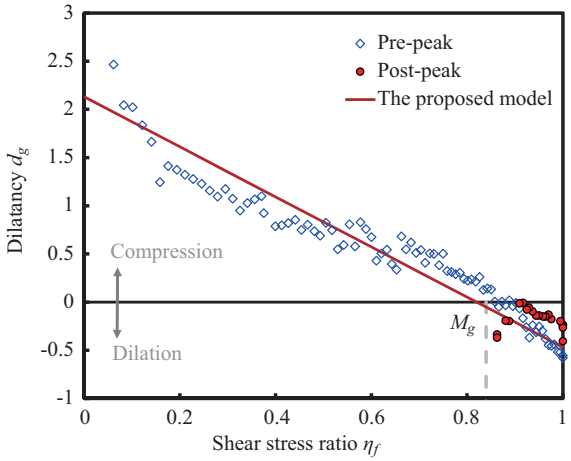


Fig.5 Variations in the dilatancy d_g under shear loading. η_f is defined as q/q_f and serves as an index of the degree of shear loading. The rhombus symbols represent the dilatancy in the pre-peak stage, and the solid circle symbols represent the dilatancy in the post-peak stage.

$$d_g = \frac{d\varepsilon_v^p}{d\gamma^p} \tag{5}$$

When the dilatancy is greater than 0, $\delta\varepsilon_v^p$ is compressive. By contrast, when the dilatancy is less than 0, $\delta\varepsilon_v^p$ is dilative. Figure 5 shows the variations of dilatancy at various shear stress ratios (η_f; $\eta_f = q/q_p$,

https://doi.org/10.1017/jmech.2017.71 Published online by Cambridge University Press

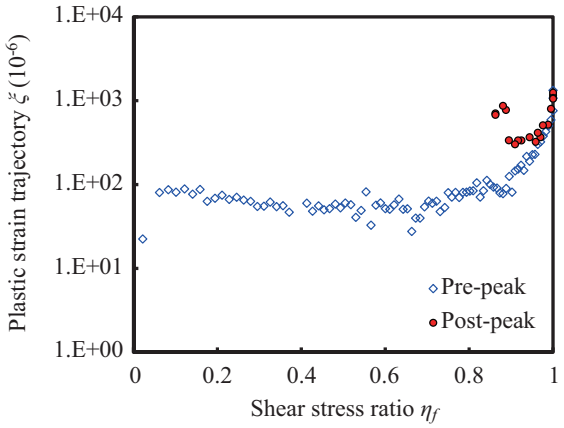
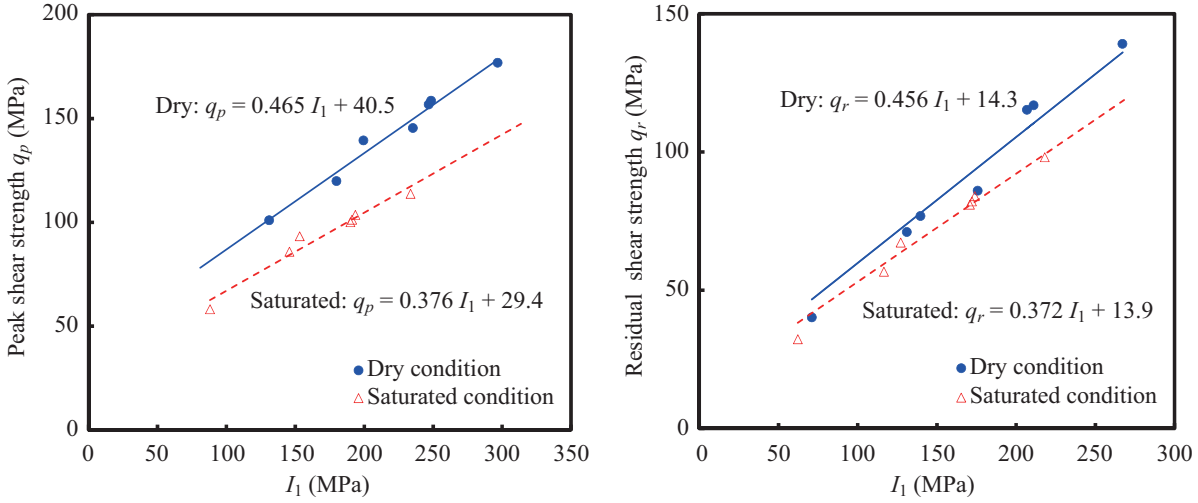


Fig. 6 Variations in the plastic strain trajectory during the CTC tests. The rhombus symbols represent the plastic strain trajectories in the pre-peak stage, and the solid circle symbols represent the plastic strain trajectories in the post-peak stage.



(a) Peak strength (b) Residual strength

Fig. 7 Failure envelopes of the studied sandstone.

$q = \sqrt{3J_2}$, and q_p is the shear strength). At a low stress ratio, the dilatancy is greater than 0 and gradually decreases with an increase in η_f. When η_f is approximately 0.85, the volumetric deformation becomes dilative. In addition, the dilatancy approaches approximately -0.58 when the loading is at the ultimate strength. Next, in the post-peak softening stage, the dilatancy begins to increase (solid circular symbols in Fig. 5). Last, the dilatancy remains at -0.37 when the loading is at the residual strength.

In addition, for the magnitude of plastic strain increment, the plastic strain trajectory ξ is defined as

$$\xi = \sqrt{\delta\varepsilon_{ij}^{p}\,\delta\varepsilon_{ij}^{p}}\ , \tag{6}$$

where $\delta\varepsilon_{ij}^{p}$ is the tensor of the plastic strain increment. Figure 6 illustrates the plastic strain trajectory per MPa change in shear stress. This figure indicates that the plastic strain occurs even for a minor degree of shearing (η_f < 0.5) and significantly increases by approximately two orders of magnitude when the failure state is approached (η_f = 0.85 – 1). Similarly, in the post-peak softening stage, ξ begins to decrease (solid circle symbols in Fig. 6) and then increases. Last, ξ remains at a high magnitude when the loading is at the residual strength. According to the tendencies of β and ξ, a constitutive model considering post-peak behavior is proposed in the following section.

3.2 Failure Envelopes

Failure envelopes of the sandstones were obtained according to the maximum strength of each test, and the residual strength envelopes were acquired on the basis of the residual strength in the post-peak softening stage (Fig. 7). The failure envelopes of sandstones under dry and saturated conditions are generally linear when ex-

https://doi.org/10.1017/jmech.2017.71 Published online by Cambridge University Press

Table 1 Material parameters for different types of sandstones associated with the proposed model.

Model properties	Parameter	MS sandstone (Dry)	MS sandstone (Saturated)	RW sandstone (Papamichos *et al*.,1998)	Greywacke (Wang *el al*., 2012)
Elastic component	b_1 (MPa)$^{-1/2}$	664×10^{-7}	300×10^{-7}	436×10^{-7}	474×10^{-7}
	b_2	10000×10^{-7}	100×10^{-7}	800×10^{-7}	1000×10^{-7}
	b_3 (MPa)$^{-1/2}$	95×10^{-7}	100×10^{-7}	250×10^{-7}	170×10^{-7}
Failure criterion	α_d	0.269	0.30	0.264	0.314
	k_d (MPa)	22.64	17.20	4.86	11.87
Plastic component	M_g	0.82	0.82	0.6	0.6
	α	1.6	1.6	0.6	1.5
	H_0 (MPa)	63240	20000	28460	39530
	β_0	0.85	1.62	1.05	0.68
	β_1	0.76	0.92	1.60	0.85
	β_2	0.50	0.67	1.00	0.66
	H_{u0} (MPa)	180000	-	-	-

pressed for stress invariants of three-dimensional stress components (Fig. 7(a)). Therefore, the linear relationship, known as the Drucker-Prager criterion (Eq. 7), is adopted:

$$q_p = \sqrt{3J_{2,f}} = \sqrt{3}(\alpha_d I_1 + k_d), \tag{7}$$

where q_p is the shear strength; J_2 is the second deviatoric stress invariant ($J_2 = \frac{1}{2} s_{ij} s_{ji}$, where s_{ij} is the deviatoric stress tensor); I_1 is the first stress invariant; and parameters α_d and k_d are the slope and cohesive interception of the failure envelope, respectively. The experimental results show that α_d of the dry specimen is higher than that of the saturated specimen. In addition, k_d of the dry specimen is greater than that of the saturated specimen. Therefore, the wetting deterioration influences both α_d and k_d.

The failure envelope expressed by Eq. 7 can be converted to the Mohr-Coulomb failure criterion by using the following relations

$$\phi = \sin^{-1}\left(\frac{3\sqrt{3}\alpha}{2+\sqrt{3}\alpha}\right), \tag{8}$$

$$c = \frac{\sqrt{3}(3-\sin\phi)k}{6\cos\phi}, \tag{9}$$

so that the friction angle ϕ and cohesion intercept c are 34.5° and 19.3 MPa under dry conditions, and 28.3° and 14.1 MPa under saturated conditions, respectively. The parameters of strength are summarized in Table 1.

For the residual strength envelopes, the envelopes under dry and saturated conditions exhibit generally linear curves, and they can be expressed using the Drucke-Prager criterion (Fig. 7(b)). Here, α_d of the residual strength is slightly lower than that of failure envelopes; however, k_d of the residual strength decrease significantly after the peak strength. In addition, α_d of the dry specimen is higher than that of the saturated specimen, whereas k_d of the dry and saturated specimens is similar. The cause of strength reduction is related to the wetting deterioration of sandstone. Wetting deterioration means a decrease in material strength and stiffness caused by water penetration. According to [20] and [21], the sandstone with greater porosity and smaller grain area ratio, such as MS sandstone, may exhibit more significant wetting deterioration. Furthermore, the softening ratio η_r is defined as the ratio between the residual strength and the peak strength (q_r/q_p). Figure 8 shows the variations of softening ratio η_r under different confining pressure. η_r under dry conditions increases from 0.4 to 0.75 with an increase in the confining stress, indicating that post-peak softening behavior becomes less apparent as the confining stress increases. A similar tendency is evident for the saturated specimen, of which η_r increases from 0.55 to 0.86 with an increase in the confining stress. Figure 9 shows the typical failure pattern of the sandstone specimen after a CTC test. A main shear fracture developed through the specimen.

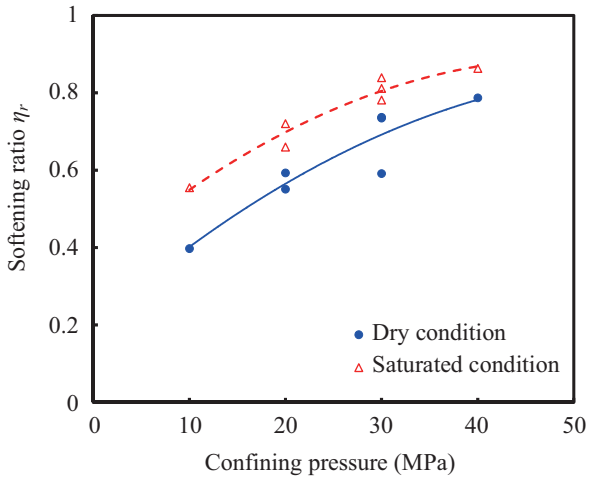


Fig. 8 Variations of softening ratio under different confining pressures.

https://doi.org/10.1017/jmech.2017.71 Published online by Cambridge University Press



Fig. 9 Failure pattern of the specimen of a CTC test under the confining pressure of 20 MPa.

4. THE PROPOSED CONSITUTIVE MODEL

According to the aforementioned deformational characteristics of sandstone, a constitutive model is proposed here. The constitutive model is based on the theories of Green elasticity and generalized plasticity, and it is modified from [19-20].

According to generalized plasticity, the total strain increment can be divided into elastic and plastic components as follows:

$$d\varepsilon = d\varepsilon^e + d\varepsilon^p, \tag{10}$$

where $d\varepsilon$, $d\varepsilon^e$, and $d\varepsilon^p$ are the increments of total, elastic, and plastic strain tensors, respectively.

The elastic and plastic strain increments can be obtained using the following equations:

$$d\boldsymbol{\varepsilon}^{\mathrm{e}} = \boldsymbol{C}^e : d\boldsymbol{\sigma} \tag{11}$$

and

$$d\boldsymbol{\varepsilon}^p = d\lambda \boldsymbol{n}_g = \frac{1}{H_{L/U}} \left(\boldsymbol{n}_{gL/U} \otimes \boldsymbol{n}\right) : d\boldsymbol{\sigma}, \tag{12}$$

where $\boldsymbol{C}^e$ is the elastic constitutive tensor, $d\boldsymbol{\sigma}$ is the increment of the stress tensor, $\boldsymbol{n}_g$ is the unit tensor defining the plastic flow direction, $\boldsymbol{n}$ represents the loading direction tensor, $d\lambda$ is a plastic scalar, and $H_{L/U}$ is the plastic modulus, which can be assumed directly without introducing a hardening rule. Subscripts L and U indicate loading and unloading, respectively.

To express the increment of stress as a function of the strain increment, Eq. (11) is inversed and expressed as

$$d\boldsymbol{\sigma} = \boldsymbol{D}^{ep} : d\boldsymbol{\varepsilon} \tag{13}$$

$$\boldsymbol{D}^{ep} = \boldsymbol{D}^e - \frac{\boldsymbol{D}^e : \boldsymbol{n}_{g_{L/U}} \otimes \boldsymbol{n} : \boldsymbol{D}^e}{H_{L/U} + \boldsymbol{n} : \boldsymbol{D}^e : \boldsymbol{n}_{g_{L/U}}},$$

where $\boldsymbol{D}^{ep}$ and $\boldsymbol{D}^e$ are the elasto-plastic and elastic matrices, respectively.

Based on this concept of generalized plasticity, the yield potential surfaces are not directly specified; however, the scalar functions for plastic modulus $H_{L/U}$ and direction tensors $\boldsymbol{n}$ and $\boldsymbol{n}_g$ are required. To incorporate the deformation characteristics of sandstone into generalized plasticity, this study proposes (and subsequently defines) the major constituents of the model, namely nonlinear elasticity, dilatancy, and plastic modulus.

4.1 Nonlinear Elastic Behavior

According to the Green elastic theory, the strain tensor is related to the derivatives of the energy density function as follows:

$$\boldsymbol{\varepsilon}^e = \frac{\partial \Omega}{d\boldsymbol{\sigma}}, \tag{14}$$

where Ω is the energy density function.

On the basis of the nonlinear elastic behavior of sandstone (Fig. 4), this study adopts the following energy density function for Ω, which has been proposed by previous studies [24]:

$$\Omega = b_1 I_1^{3/2} + b_2 I_1^{-1} J_2 + b_3 J_2, \tag{15}$$

where b_1, b_2, and b_3 are material parameters, I_1 is the first stress invariant ($I_1 = \sigma_{kk} = 3p$), and J_2 is the second deviatoric stress invariant. After substituting Eq. 15 into Eq. 14, the elastic strain tensor ε_{ij}^e is obtained as follows:

$$\varepsilon_{ij}^e = \frac{\partial \Omega}{\partial \sigma_{ij}} = \left(\frac{3}{2} b_1 I_1^{1/2} - b_2 I_1^{-2} J_2 + J_2\right)\delta_{ij} + (b_2 I_1^{-1} + b_3) s_{ij}, \tag{16}$$

where δ_{ij} is the Kronecker delta tensor. Greater values of b_1, b_2, and b_3 indicate that an increasing elastic strain is generated by the model. Equation (16) is derived using a rigorous elastic theory and satisfies the principle of thermodynamics, indicating that energy is conserved during any type of loading.

From Eq. (16), the elastic strains induced by hydrostatic pressure and shear stress can be obtained as Eqs. (17) and (18).

$$\varepsilon_v^e = \varepsilon_{kk}^e = \frac{9}{2} b_1 \sqrt{I_1} - 3 b_2 \left(\frac{\sqrt{J_2}}{I_1}\right)^2 \tag{17}$$

$$\gamma^e = \frac{2}{\sqrt{3}} \left(b_2 I_1^{-1} + b_3\right) \sqrt{J_2} \tag{18}$$

where ε_v^e and γ^e are the elastic volumetric strain and shear strain, respectively. In Eq. (17), the volumetric strain possesses nonlinear behavior and shear stress induces elastic volumetric deformation. Equation (18) shows that the elastic shear stiffness increases with increasing hydrostatic pressure applied.

4.2 Dilatancy and Viscoplastic Flow

To evaluate the stress–dilatancy relationship, this study adopts a function similar to that used in [13], relating the dilatancy d_g and stress ratio η_f as follows:

https://doi.org/10.1017/jmech.2017.71 Published online by Cambridge University Press

$$d_g = \frac{d\varepsilon_v^p}{d\gamma^p} = (1+\alpha)(M_g - \eta_f), \tag{19}$$

where $d\varepsilon_v^p$ and $d\gamma^p$ are the incremental plastic volumetric and shear strains, respectively, and M_g is the threshold of shear dilation in the triaxial plane. When $\eta_f = M_g$, $d_g = 0$ and volumetric strain does not occur. The deformation mode converts from compression to dilation when $\eta_f > M_g$. The variable α is a model parameter.

According to [13], the plastic flow direction under loading and unloading $n_{gL/U}$ in the triaxial space is

$$\boldsymbol{n}_{\boldsymbol{gL/U}} = \left(\frac{d_g}{\sqrt{1+d_g^2}}, \frac{1}{\sqrt{1+d_g^2}} \right)^T, \tag{20}$$

Similarly, the loading direction tensor can be expressed as

$$\boldsymbol{n} = \left(\frac{d_f}{\sqrt{1+d_f^2}}, \frac{1}{\sqrt{1+d_f^2}} \right)^T, \tag{21}$$

where $d_f = (1 + \alpha)(M_f - \eta)$, and M_f is a material parameter.

According to [6] and [7], the triaxial results showed that the plastic potential surface of sandstone coincides with the yield surface in the pre-peak stage. Therefore, the associated flow rule, $\boldsymbol{n} = \boldsymbol{n}_{\boldsymbol{gL/U}}$ and $M_f = M_g$, can be used when formulating the constitutive model for sandstone. To consider post-peak behavior, $\boldsymbol{n}$ might differ from $\boldsymbol{n}_{gL/U}$, indicating that the non-associated flow rule is followed. However, Fig. 5 indicates that the dilatancy at the residual strength is close to that at the peak strength. To simplify the proposed model, the associated flow rule is still obeyed hereafter.

4.3 Plastic Modulus for Loading and Unloading

The original generalized plasticity model showed its capability in predicting the post-peak behavior of soils. To consider the post-peak behavior of sandstone, the plastic modulus H_L becomes negative after the peak is reached. Therefore, the function of the plastic modulus for sandstone under loading can be expressed as

$$H_L = H_0 \sqrt{p'/p_{atm}} H_f (H_s + H_v), \tag{22}$$

$$H_f = (1-\eta^2), \tag{23}$$

$$H_s = \exp\left[-\left(\frac{p'}{p_{atm}} \right)^{\beta_0} \xi_s \right], \tag{24}$$

$$H_v = \beta_1 - \frac{q}{p'}\beta_2, \tag{25}$$

where H_0 is the multiplication factor related to the initial plastic modulus; H_f, H_s, and H_v are plastic coefficients; p_{atm} is the atmospheric pressure; β_0, β_1, and β_2 are material parameters; and $\xi_s = \int |d\gamma^p| = \int d\xi_s$ is the accumulated plastic shear strain.

To consider that the plastic strain occurs during the unloading process, the unloading plastic modulus H_u can be expressed as

$$H_u = H_{u0}, \tag{26}$$

where H_{u0} is a material parameter.

4.4 Parameter Determination

A total of 12 material parameters (b_1, b_2, b_3, α_d, k_d, M_g, α, H_0, β_0, β_1, β_2, and H_{u0}) can be determined using the experimental results. The influence of these parameters on deformation behavior is relatively straightforward. Variables b_1, b_2, and b_3 are elastic parameters; α_d and k_d are strength parameters; M_g and α are parameters related to the stress–dilatancy relationship; H_0, β_0, β_1, and β_2 are parameters representing the variation in the loading plastic modulus; and H_{u0} is a parameter related to the unloading plastic modulus. To obtain these parameters, conducting three triaxial tests with various hydrostatic pressures is recommended. The difference in the hydrostatic pressures should be sufficient to encompass the range of stress levels of interest. Furthermore, a test at the medium hydrostatic pressure should be conducted with multiple unloading–reloading procedures to distinguish and separate elastic deformation from total deformation. The following subsection describes the determination of each parameter.

4.4.1 Elastic Parameters b_1, b_2, and b_3

Parameter b_1 controls the interaction between the hydrostatic stress and the elastic volumetric strain. This parameter can be determined by fitting the elastic volumetric unloading–reloading regression curve under hydrostatic pressure stage and by using Eq. (17) to obtain the value of b_1. Parameter b_2 is related to the coupling between the shear stress and elastic dilation and can be obtained by fitting the unloading–reloading regression curve with normalized stress ($\sqrt{J_2}/I_1$) under shear stress stage and by using Eq. (18). After obtaining parameter b_2, parameter b_3 can be obtained by fitting the shear stress and the elastic shear strain curve and by using Eq. (18).

4.4.2 Strength Parameters α_d and k_d

Parameters α_d and k_d can be determined by fitting the failure envelope of sandstone (Fig. 7) by using Eq. (7).

4.4.3 Stress–Dilatancy Parameters M_g and α

Term M_g is determined using the plot of the threshold of dilatancy versus the stress ratio (Fig. 5). Alternatively, this parameter can be obtained directly from the plastic volumetric strain curve under shear loading. Parameter α is determined by fitting the curve of the plot of dilatancy versus the stress ratio (Fig. 5). Parameter α can also be obtained from the slope of the plot of dilatancy d_g versus (M_g/η).

4.4.4 Loading Plastic Modulus Parameters H_0, β_0, β_1, and β_2

The initial plastic modulus parameter H_0 can be de-

https://doi.org/10.1017/jmech.2017.71 Published online by Cambridge University Press

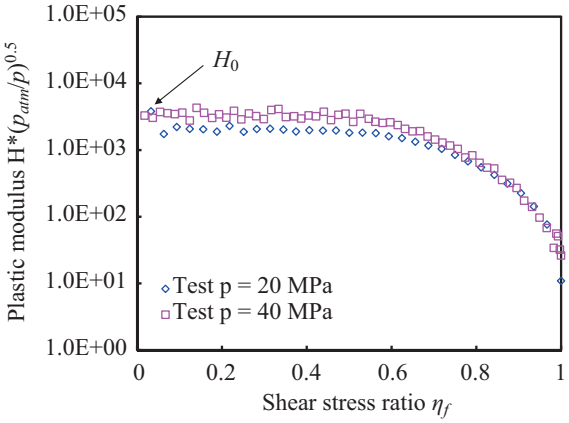
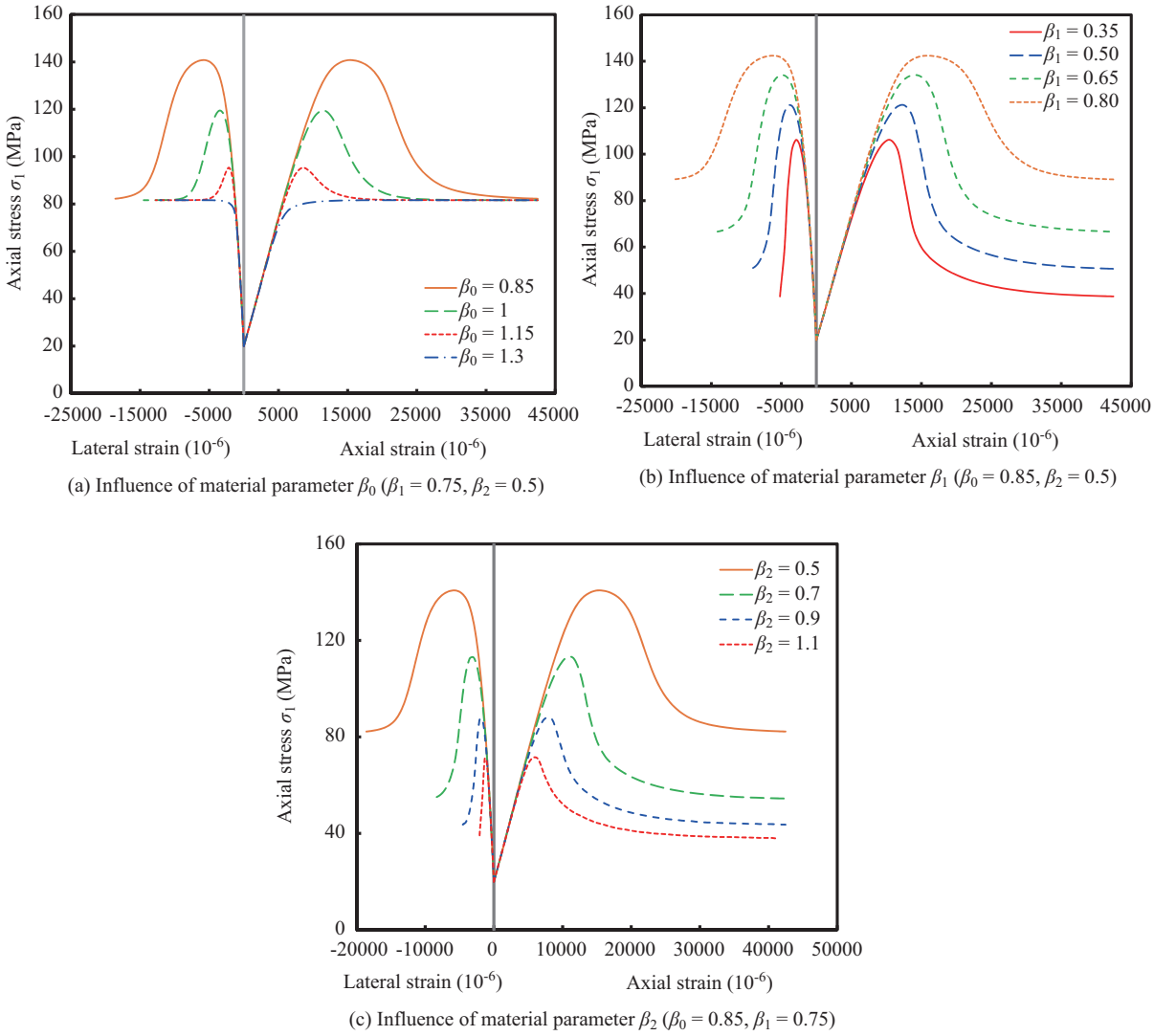


Fig. 10 Variations of normalized plastic modulus $H_L\sqrt{p_{atm}/p'}$ under shear loading with different confining pressures.



(a) Influence of material parameter β_0 ($\beta_1 = 0.75$, $\beta_2 = 0.5$)

(b) Influence of material parameter β_1 ($\beta_0 = 0.85$, $\beta_2 = 0.5$)

(c) Influence of material parameter β_2 ($\beta_0 = 0.85$, $\beta_1 = 0.75$)

Fig. 11 Influence of material parameters β_0, β_1, and β_2 on post-peak deformation.

termined on the basis of the plot of the initial stress ratio in the normalized plastic modulus $H_L\sqrt{p_{atm}/p'}$ versus the stress ratio (Fig. 10) or by fitting the initial slope of both the plastic shear and the volumetric strain curves under shear loading.

Parameter β_0 controls the degree of post-peak plastic modulus degradation; however, it does not affect the magnitude of the residual strength. The influence of β_0 on post-peak deformation is shown in Fig. 11(a). As β_0

https://doi.org/10.1017/jmech.2017.71 Published online by Cambridge University Press

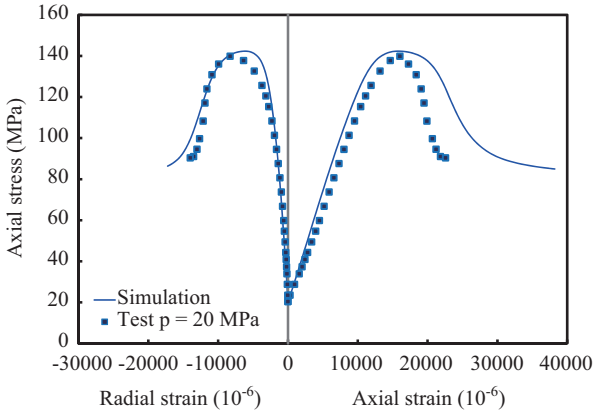


Fig. 12 Simulation of the complete stress–strain relationships of MS sandstone under a confining pressure of 20 MPa.

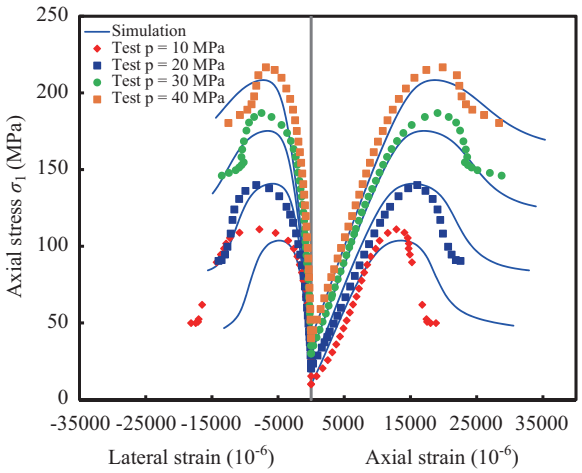


Fig. 13 Simulation of the CTC tests of MS sandstone under dry condition.

increases, the degree of plastic modulus degradation becomes insignificant, that is, deformation is more ductile. Parameter β_1 influences the magnitude of the residual strength (Fig. 11(b)); a higher β_1 induces a higher residual strength. Parameter β_2 controls the influence of the stress ratio q/q' on the plastic modulus. As β_2 increases, the peak and residual strengths decrease and modulus degradation becomes more significant (Fig. 11(c)). Parameters β_0, β_1, and β_2 can be determined by matching the post-peak curve of the experimental data. The other material parameters in Fig. 11 are based on those of MS sandstone (Table 1).

4.4.5 Unloading plastic modulus parameter H_{u0}

Parameter H_{u0} can be determined by matching the slopes of the unloading curves.

Using these procedures, the corresponding material parameters of MS sandstone in dry conditions can be obtained from one triaxial test with multiple unloading–reloading under a hydrostatic pressure of 20 MPa. Table 1 presents a summary of these parameters.

5. MODEL VALIDATION AND SIMULATON

To assess the validity of the proposed model, one triaxial test under a hydrostatic pressure of 20 MPa was first simulated. Furthermore, the proposed model with the same set of material parameters was used to predict deformation behavior under different levels of hydrostatic stress (Table 1). The proposed model was the used to simulate the tests under saturated conditions and tests of other sandstones.

5.1 Triaxial Tests of MS Sandstone

To verify the proposed model and determine the material parameters, Fig. 12 shows the simulated and measured strain in a triaxial test. As shown, the axial and radial deformation curves are consistent with actual behavior. The simulation results resemble the experimen

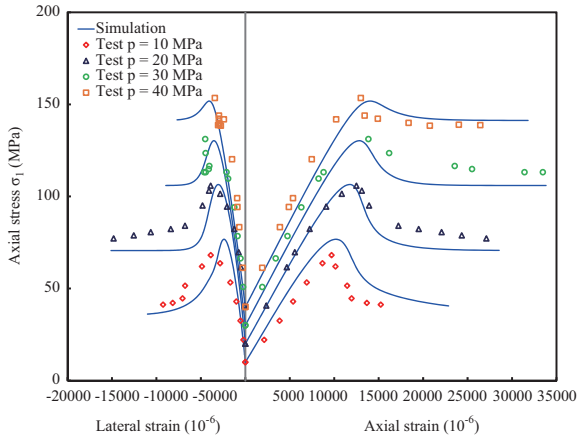


Fig. 14 Simulation of the CTC tests of MS sandstone under saturated condition.

tal results in both tendency and magnitude. To further evaluate the predictive capability of the proposed model under different levels of hydrostatic stress, four triaxial tests of dry MS sandstone at hydrostatic stress levels ranging from 10 to 40 MPa were simulated. Figure 13 illustrates these simulation results. The simulated deformation modulus at the pre-peak stage increases with an increase in the applied confining pressure. In the post-peak stage, the magnitude of post-peak softening decreases with an increase in the confining pressure. The curves of the simulated axial and radial strain under various hydrostatic stress conditions reasonably reflect the tendencies of the experimental data. In addition, the simulation results of the triaxial tests under saturated conditions are shown in Fig. 14. The simulation results are in satisfactory agreement with the experimental data.

5.2 Other Sandstones

To consider the variety of sandstone, the deformational behavior of two other sandstones, Red Wildmoor (RW) sandstone and Huabei greywacke, was simulated.

https://doi.org/10.1017/jmech.2017.71 Published online by Cambridge University Press

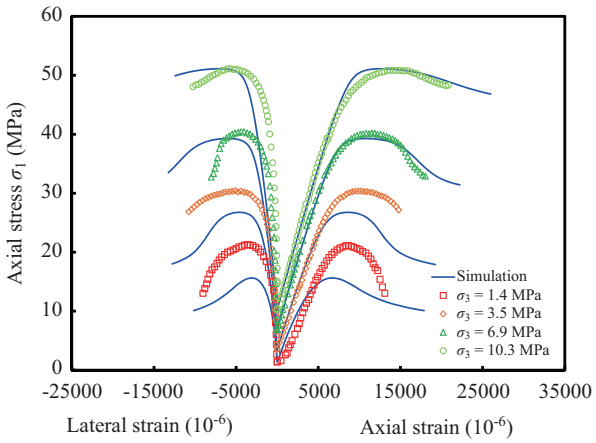


Fig. 15 Simulation of the stress–strain curves of RW sandstone (experimental data: Papamichos *et al*., 2010).

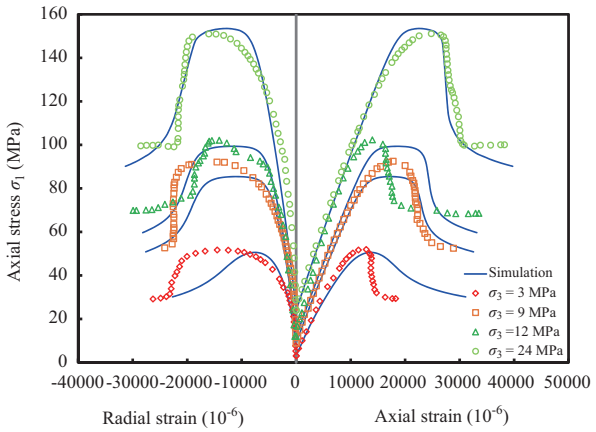


Fig. 16 Simulation of the stress–strain curves of Huabei greywacke (experimental data: Wang *et al*., 2012).

The experimental data were obtained from [9] and [10]. RW sandstone is a weak Triassic sandstone found in Bromsgrove, United Kingdom. It has a porosity of 25.8% and a mean grain diameter of 0.107 mm. The uniaxial compressive strength is 21.7 MPa under dry conditions and 9.4 MPa under humid conditions. To evaluate the validity of the proposed model, four triaxial tests of the RW sandstone from [9] were simulated and the corresponding parameters are listed Table 1. Figure 15 shows the complete stress–strain curves of the RW sandstone under confining pressures from 1.4 to 10.3 MPa. Predictions are mostly consistent with the experimental results, except that the discrepancies of the simulation under lower confining pressure (1.4 MPa and 3.5 MPa) are somewhat less than the actual curves. The discrepancies occur because the linear failure criterion (Eq. 7) underestimates the shear strength at low hydrostatic pressure and the values of parameters β_1, and β_2 are too low to reflect the high softening ratio. Increasing the shear strength and the values of β_1, and β_2 may improve the discrepancies at low hydrostatic pressure, but it may overestimate the strength and softening ratio at high hydrostatic pressure. Despite this, the predicted tendency is still reasonable with the experimental results.

Huabei greywacke is a Permian rock in China, and [10] performed a series of triaxial tests under confining pressures from 3 to 24 MPa. The set of material parameters for Huabei greywacke is listed in Table 1. Figure 16 illustrates comparisons between the results of simulations and experiments at different hydrostatic stress levels. Though the discrepancy of the simulation occur at lower confining pressure, the overall simulation reasonably agrees with the measured results. In summary, the tests of different types of sandstones at varying confining stress levels and water contents indicate that the proposed model can provide reasonable simulations in the aforementioned situations.

6. SUMMARY AND CONCLUSIONS

To explore the elasto-plastic characteristics of sandstone in the post-peak stage, a series of strain-controlled triaxial tests were conducted under different confining pressures. The experimental results reveal that the elastic and plastic deformation of sandstone exhibits the following characteristics:

(1) Nonlinear elastic behavior is evident in both the pre-peak and post-peak stages.

(2) The plastic angle β increases with an increase in the shear stress ratio, and it approaches the highest value when loading is at the ultimate strength. Subsequently, in the post-peak softening stage, β begins to decrease; however, it increases after softening ceases. Last, β remains fixed when loading is at the residual strength.

(3) The plastic strain trajectory ξ increases with an increase in the shear stress ratio. In the post-peak softening stage, ξ begins to decrease and then increases. Last, ξ remains at a high magnitude when loading is at the residual strength.

(4) The shear stress ratio between the residual strength and the peak strength increases with an increase in the confining stress, indicating that post-peak softening behavior becomes less significant as the confining stress increases.

According to post-peak behavior, a constitutive model based on nonlinear elasticity and generalized plasticity is proposed. This proposed model is characterized by the following features: (1) Nonlinear elasticity is observed under hydrostatic and shear loading; (2) the associated flow rule is followed; (3) substantial plastic deformation occurs during shear loading; and (4) post-peak softening behavior is accurately predicted. The model requires twelve material parameters, three for elasticity and nine for plasticity. The model was validated by comparing the triaxial test results of the MS sandstone at different hydrostatic pressures under dry and saturated conditions. The model was also adopted to simulate the deformation behavior of two other sandstones (RW sandstone and Huabei greywacke). Furthermore, the constitutive model has been incorporated into the finite element program ABAQUS and can be applied for the analysis of

https://doi.org/10.1017/jmech.2017.71 Published online by Cambridge University Press

rock engineering in the future.

ACKNOWLEDGEMENTS

The research is supported by the National Science Council of Taiwan, Grant no. NSC 101-2628-E-390-001-MY2, and the Ministry of Science and Technology of Taiwan, Grant no. MOST 103-2625-M-390-004.

REFERENCES

1. Jeng, F. S., Weng, W. C., Huang, T. H. and Lin, M. L., "Deformational Characteristics of Weak Sandstone and Impact to Tunnel Deformation," *Tunnelling and Underground Space Technology*, **17**, pp. 263-264 (2002).
2. Goodman, R. E., *Introduction to Rock Mechanics*, 2nd Edition, John Wiley & Sons, New York (1989).
3. Zhang, J., Wong, T. F. and Davis, D. M., "Micromechanics of Pressure-Induced Grain Crushing in Porous Rocks," *Journal of Geophysical Research*, **95**, pp. 341-352 (1990).
4. Zimmerman, R. W., *Compressibility of Sandstones*, Elsevier, Amsterdam (1991).
5. Bernabe, Y., Fryer, D. T. and Shively, R.M., "Experimental Observations of the Elastic and Inelastic Behaviour of Porous Sandstones," *Geophysical Journal International*, **117**, pp. 403-418 (1994).
6. Bésulle, P., Desrues, J. and Raynaud, S., "Experimental Characterization of the Localisation Phenomenon Inside a Vosges Sandstone in a Triaxial cell," *International Journal of Rock Mechanics and Mining Sciences and Geomechanics Abstracts*, **37**, pp. 1223-1237 (2000).
7. Weng, M. C., Jeng, F. S., Huang, T. H. and Lin, M. L., "Characterizing the Deformation Behavior of Tertiary Sandstones," *International Journal of Rock Mechanics and Mining Sciences*, **42**, pp. 388-401 (2005).
8. Tsai, L. S., Hsieh, Y. M., Weng, M. C., Huang, T. H. and Jeng, F. S., "Time-Dependent Deformation Behaviors of Weak Sandstones," *International Journal of Rock Mechanics and Mining Sciences*, **45**, pp. 144-154 (2008).
9. Papamichos, E. *et al*., "Constitutive Testing of Red Wildmoor Sandstone," *Mechanics of Cohesive-Frictional Materials*, **5**, pp. 1-40 (2000).
10. Wang, D., Liu, C. W., Wang, D., Cao, L. and Du, X. L., "Failure Prediction and Post-Failure Behavior of Typical Rock under Triaxial Compression," *Journal of Southwest Jiaotung University*; **47**, pp. 90-96 (2012). (In Chinese)
11. Zienkiewicz, O. C. and Mroz, Z., "Generalized Plasticity Formulation and Applications to Geomechanics," *Proceedings of Mechanics of Engineering Materials*, Desai, C. S., Gallagher, R. H. (eds), Wiley, New York, pp. 655-679 (1984).
12. Pastor, M. and Zienkiewicz, O. C., "A Generalized Plasticity, Hierarchical Model for Sand under Monotonic and Cyclic Loading," *Proceedings of 2nd International Symposium on Numerical Models in Geomechanic*, Ghent, pp. 131-149 (1986).
13. Pastor, M., Zienkiewicz, O. C. and Chan, A. H. C., "Generalized Plasticity and the Modelling of Soil Behavior" *International Journal for Numerical and Analytical Methods in Geomechanics*, **14**, pp. 151-190 (1990).
14. Pastor, M., Zienkiewicz, O. C., Guang-Duo, X. and Peraire, J., "Modelling of Sand Behaviour: Cyclic Loading, Anisotropy and Localization," *Modern Approaches to Plasticity*, Kolymbas, D. (eds), Springer, Berlin (1992).
15. Bolzon, G., Schrefler, B. A. and Zienkiewicz, O. C., "Elasto–Plastic Constitutive Laws Generalised to Partially Saturated States," *Géotechnique*, **46**, pp. 279-289 (1996).
16. Ling, H. I. and Liu, H., "Pressure-Level Dependency and Densification Behavior of Sand through a Generalized Plasticity Model," *Journal of Engineering Mechanics*, **129**, pp. 851-860 (2003).
17. Manzanal, D., Fernández Merodo, J. A. and Pastor, M., "Generalized Plasticity State Parameter-Based Model for Saturated and Unsaturated Soils. Part 1: Saturated State," *International Journal for Numerical and Analytical Methods in Geomechanics*, **35**, pp. 1347-1362 (2011).
18. Manzanal, D., Pastor, M. and Fernández Merodo, J. A., "Generalized Plasticity State Parameter-Based Model for Saturated and Unsaturated Soils. Part II: Unsaturated soil modeling," *International Journal for Numerical and Analytical Methods in Geomechanics*, **35**, pp. 1899-1917 (2011).
19. Weng, M. C. and Ling, H. I., "Modeling the Behavior of Sandstone Based on Generalized Plasticity Concept," *International Journal for Numerical and Analytical Methods in Geomechanics*, **37**, pp. 2154-2169 (2013).
20. Weng, M. C., "A Generalized-Plasticity Based Model for Sandstone Considering Time-Dependent Behavior and Wetting Deterioration," *Rock Mechanics and Rock Engineering*, **47**, pp. 1197-1209 (2014).
21. Jeng, F. S., Weng, W. C., Lin, M. L. and Huang, T. H., "Influence of Petrographic Parameters on Geotechnical Properties of Tertiary Sandstones from Taiwan," *Engineering Geology*, **73**, pp. 71-91 (2004).
22. Weng, M. C. and Li, H. H., "Relationship between the Deformation Characteristics and Microscopic Properties of Sandstone Explored by the Bonded-Particle Model," *International Journal of Rock Mechanics and Mining Sciences*, **56**, pp. 33-43 (2012).

https://doi.org/10.1017/jmech.2017.71 Published online by Cambridge University Press

23. *Rock Characterization Testing and Monitoring-ISRM Suggested Methods*, Pergamon, New York (1981).
24. Weng, M. C., Tsai, L. S., Hsieh, Y. M. and Jeng, F. S., "An Associated Elastic-Viscoplastic Constitutive Model for Sandstone Involving Shear-Induced Volumetric Deformation," *International Journal of Rock Mechanics and Mining Sciences*, **47**, pp. 1263-1273 (2010).

(Manuscript received February 13, 2017,
accepted for publication July 3, 2017.)

https://doi.org/10.1017/jmech.2017.71 Published online by Cambridge University Press